Pure Appl. Geophys. 173 (2016), 1847–1858

DOI 10.1007/s00024-016-1305-0

Pure and Applied Geophysics

A Study of the 2015 M_w 8.3 Illapel Earthquake and Tsunami: Numerical and Analytical Approaches

Mauricio Fuentes,[1] Sebastián Riquelme,[2] Gavin Hayes,[3] Miguel Medina,[1] Diego Melgar,[4] Gabriel Vargas,[5] José González,[5] and Angelo Villalobos[5]

Abstract—The September 16, 2015 Illapel, Chile earthquake triggered a large tsunami, causing both economic losses and fatalities. To study the coastal effects of this earthquake, and to understand how such hazards might be accurately modeled in the future, different finite fault models of the Illapel rupture are used to define the initial condition for tsunami simulation. The numerical code Non-hydrostatic Evolution of Ocean WAVEs (NEOWAVE) is employed to model the tsunami evolution through the Pacific Ocean. Because only a short time is available for emergency response, and since the earthquake and tsunami sources are close to the coast, gaining a rapid understanding of the near-field run-up behavior is highly relevant to Chile. Therefore, an analytical solution of the 2 + 1 D shallow water wave equations is considered. With this solution, we show that we can quickly estimate the run-up distribution along the coastline, to first order. After the earthquake and tsunami, field observations were measured in the surrounded coastal region, where the tsunami resulted in significant run-up. First, we compare the analytical and numerical solutions to test the accuracy of the analytical approach and the field observations, implying the analytic approach can accurately model tsunami run-up after an earthquake, without sacrificing the time necessary for a full numerical inversion. Then, we compare both with field run-up measurements. We observe the consistency between the two approaches. To complete the analysis, a tsunami source inversion is performed using run-up field measurements only. These inversion results are compared with seismic models, and are shown to capture the broad-scale details of those models, without the necessity of the detailed data sets they invert.

Key words: Tsunami, Illapel earthquake, inversion, run-up.

1. Introduction

The Peru–Chile subduction zone has historically released approximately 35–40 % of the total seismic moment from global earthquakes over the past century or more (Pacheco and Sykes 1992; Scholz 2002). Three of the last eight global great-sized earthquakes ($M_w > 8$) have been located in Chile, all in the last 6 years (Maule 2010; Iquique 2014; Illapel 2015). These events each produced tsunamis, ranging in size from moderate to large. Therefore, to mitigate the impact of these disasters, it is crucial to understand tsunami propagation, shoaling and run-up. The recent Illapel earthquake (September 16, 2015) presents an ideal opportunity to understand the source process and how this in turn affects run-up behavior.

The September 16, 2015 M_w 8.3 Illapel event occurred in the same region as the 1943 Illapel earthquake, which was estimated as an M_w 7.9 event with an under-thrust mechanism (Beck *et al.* 1998). The Illapel earthquake has been proposed to be a repeat of the 1943 event (e.g., Heidarzadeh *et al.* 2015). However, comparisons of source time functions show that the 2015 event was much larger than the 1943 earthquake; the 1943 event had a duration of 24–28 s (Beck *et al.* 1998) and the source time function for the 2015 Illapel earthquake indicates a rupture duration of about 140 s (United States Geological Survey—USGS, http://earthquake.usgs.gov). Also, the 2015 tsunami was larger, reaching a maximum run-up of 11 m, while the 1943 event had a run-up of 4–5 m (Beck *et al.* 1998). For the 1943 earthquake, the centroid depth is located between 10 and 30 km (Beck *et al.* 1998). The centroid depth of the recent event is located at 18 km (gCMT). Given

[1] Department of Geophysics, University of Chile, Santiago, Chile. E-mail: mauricio@dgf.uchile.cl
[2] National Seismological Center, University of Chile, Santiago, Chile.
[3] National Earthquake Information Center, U.S. Geological Survey, Golden, CO, USA.
[4] Berkeley Seismological Laboratory, University of California Berkeley, Berkeley, CA, USA.
[5] Department of Geology, University of Chile, Santiago, Chile.

these differences, one can assume that these two events did not break the same part of the plate interface. This assumption is supported by the fact that high-frequency energy and lower-magnitude rupture have been observed in association with the deeper portion of the subduction interface, while tsunamigenic earthquakes typically break the upper (shallow) portion with larger magnitudes and lower-frequency energy (Lay and Kanamori 2011). Observations during recent earthquakes suggest that those phenomena can be associated with rupture on different parts of the megathrust (Lay *et al*. 2012). Run-up observations (Table 2) from the 2015 event also clearly showed that the recent tsunami was far larger than its 1943 counterpart. Therefore, from this comparison, one can conjecture that the 1943 earthquake mainly broke the deeper portion of the subduction interface (Beck *et al.* 1998). Understanding the differences between these possibilities is of significant importance for hazard characterization and response in this region.

In the Illapel region, and for the 2015 earthquake in particular, tsunami hazard is also elevated as a result of subduction zone and rupture morphology. The distance between the trench and the coast here varies between 80 and 100 km; this is shorter than other parts of Chile, where trench-to-coast distances of 120–140 km are more typical. Furthermore, the down-dip limit projection of the seismic rupture onto the surface, which defines the hinge line in the uplift/subsidence pattern, is located near the coast. As illustrated by Omira *et al*. (2016), who have studied this feature for the most recent major tsunamis along the Perú–Chile trench, this feature caused uplift along the shoreline during the Illapel earthquake. Together, these two observations result in a reduced arrival time of the tsunami at the coast. Fieldwork conducted as part of this study is consistent with the fact that the first wave was reported between 5 and 7 min after the origin time of the earthquake. This is in agreement with the post-tsunami survey conducted by Contreras-Lopez *et al*. (2016).

Such qualitative observations make it necessary to understand the run-up behavior for the 2015 event and, in particular, to ascertain whether the associated tsunami can be rapidly and accurately modeled. From our observations, we can propose a source model and then compare it with validated finite fault inversions. These analyses allow us to have a better understanding of the tsunami generation and whether this is truly a repeated earthquake or not.

In this study, an inversion of near-field run-up observations is used to obtain a slip distribution of the Illapel earthquake without seismological or tsunami records. Also, analytical techniques are introduced to quickly estimate the run-up distributions. Numerical simulations are used to compare both finite fault models (FFMs) with the run-up observations in the near field. Together, our results indicate that (1) inversions of run-up observations recover the bulk characteristics of the earthquake rupture, and (2) we can model tsunami run-up accurately with analytic approaches. Given analytic approaches are computationally much more straightforward than their more traditional numeric counterparts, this implies that we can model tsunamis with sufficient precision for warning purposes, very quickly after an FFM is available.

1.1. Previous studies

Different authors have studied the characteristics of the Illapel earthquake and tsunami. Tang et al. (2016) estimated the 2015 Illapel tsunami energy to be 7.9 x 1013 J using full-wave inversion, concluding that the main excitation of the tsunami had an area of 100–200 km long and 100 km wide close to the trench; their results are in agreement with seismological inversions (e.g. Ye et al. 2015; Melgar et al. 2016). Calisto *et al*. (2016) made an analysis of the tsunami signals (DART buoys and tide gauges) from three different faults models, finding that those signals are different in the near field, but in the far field, sources are equivalent in terms of amplitude and arrival time. Aranguiz *et al*. (2016) conducted a post-tsunami survey and modeled the seismic source with a P-wave teleseismic inversion. Despite good agreement between modeled and measured data, their seismic source cannot correctly explain the locations of peak run-up observations. Therefore, more sophisticated data and techniques are needed to generate an FFM that accounts for maximum tsunami heights.

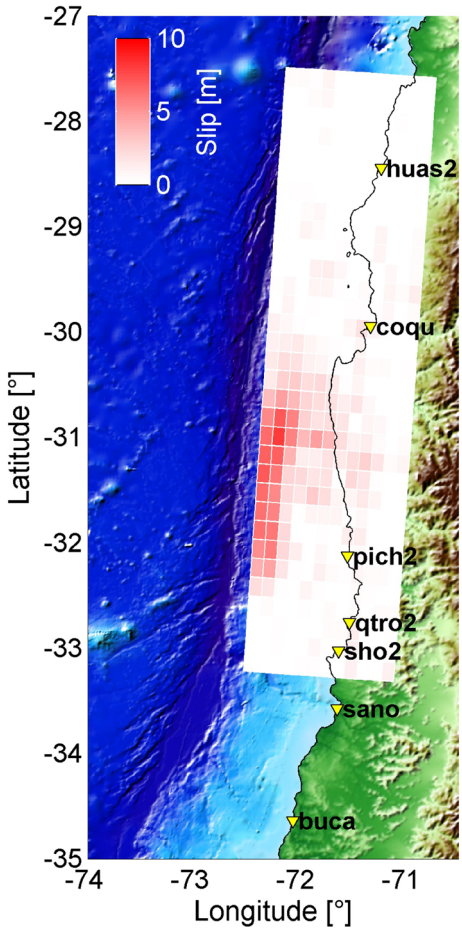

Figure 1
Slip distribution obtained from an inversion of teleseismic P-waves, SH-waves, and surface waves (USGS, http://earthquake.usgs.gov/earthquakes/eventpage/us20003k7a#scientific_finite-fault)

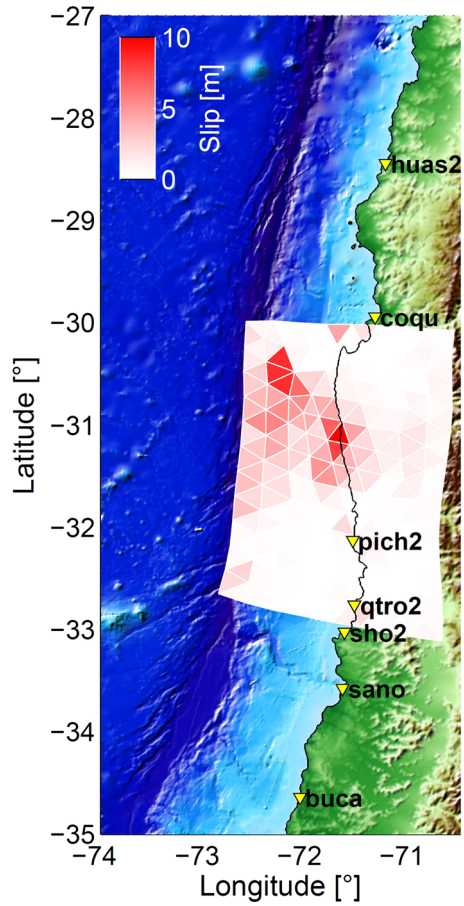

Figure 2
Slip distribution obtained from a joint inversion of tsunami tide gauge + high-rate GPS + regional strong motion records + InSAR data (Melgar *et al.* 2016)

2. *Slip Distribution Solution*

Many different approaches exist to generate a FFM. Here, we consider two inversions provided by different algorithms with different data.

2.1. *USGS Solution*

This model utilizes teleseismic data to rapidly perform an inversion in the wavelet domain (Ji *et al.* 2002). The resulting FFM for the Illapel earthquake (Fig. 1; USGS event pages, http://earthquake.usgs.gov) shows a rupture concentrated in the shallower part of the subduction interface with a seismic moment release of 3.2e + 28 dyne.cm ($M_w = 8.3$), which qualitatively agrees with the large tsunami. The source time function is 140 s in duration, initiated by a foreshock of M_w 7.2 in the first 20 s (http://earthquake.usgs.gov/learn/topics/Coquimbo_Educational_Slides.pdf). The maximum slip according to this model is $\sim$8 m.

2.2. *Berkeley Solution*

The Berkeley model employs a regional kinematic rupture from the joint inversion of regional high-rate GPS and strong motion records, local tide gauges and Sentinel-1A Interferometric Synthetic Aperture Radar (InSAR) data (Melgar *et al.* 2016).

Table 1

Comparison of both models tested

Parameters	USGS model	Berkeley model
Number of elements	384	223
Mesh type	Planar	3D triangular
Seismic moment (Nm)	3.2390×10^{21}	3.7023×10^{21}
Data type used	Teleseismic broadband P waveforms, broadband SH waveforms, and long period surface waves	Teleseismic broadband P waveforms, high-rate GPS records, strong motion records, tide gauges records, ascending and descending passes of Sentinel-1A satellite
Maximum slip (m)	8.0	10.7
Maximum slip location	(−72.2177°, −31.0743°, −5.2 km)	(−71.6741°, −31.1029°, −27.7 km)
Maximum run-up (m)	6.8	10.9
Maximum run-up location	(−71.519192°, −31.917594°)	(−71.688404°, −30.433063°)

The resulting model indicates that slip initiated at ∼30 km depth and propagated up dip and down dip at ∼2.2 km/s. Upon reaching ∼18 km depth, the rupture slowed down substantially to ∼1.6 km/s and propagated all the way to the trench (Fig. 2). The shallow slip generated a significant tsunami with modeled tide gauge amplitudes of up to 10 m. Tsunami arrivals to the near-source coastlines were recorded within 15 min of rupture initiation. The maximum slip obtained from this model is ∼11 m.

3. Tsunami Modeling

3.1. Numerical Modeling and Setup

The code NEOWAVE is used to numerically simulate the propagation and run-up of the tsunami (Yamazaki *et al.* 2009, 2011). NEOWAVE is a FORTRAN code based on a staggered nested grid scheme of finite differences, which solves the non-linear shallow water equations, including non-hydrostatic pressure to model weakly dispersive waves. Flow discontinuities are handled by a momentum conservation scheme. The runup and inundation, if possible, are computed with a wet–dry algorithm that accounts for a moving boundary condition.

Because of the large differences between tsunami and seismic rupture velocities, one can consider the initial condition as an instantaneous transfer from the seafloor to the sea surface, with null initial horizontal velocity field. This is commonly called "passive tsunami generation". An FFM is used to model sea floor uplift with Okada's equations (Okada 1985). This is then used as the initial condition for the tsunami problem. A summary of both models used as initial conditions are detailed in Table 1.

We set up the computation domain [95°W–69°W; 46°S–16°S] with a grid step of 30 arc seconds to follow GEBCO bathymetry (http://www.gebco.net/). The simulation is made for 6 h with a time step of 1 s. These step sizes were selected to ensure the stability of the numerical method by satisfying the CFL condition for convergence. With our available computational power, we can generate ten simulations of 6 h of tsunami time in around 12 h.

3.2. Analytical Modeling

Because obtaining a quick estimation of potential run-up is crucial for operational emergency management decisions, we also include an analytical computation of the tsunami run-up (i.e., rapid, available within a few seconds of FFM). This approach employs the analytical solution derived in Fuentes *et al.* (2013),

$$\mathcal{R}(y) = \mathcal{R}_0 f(p_0)\sqrt{\sin(\theta)}, \qquad (1)$$

where $\mathcal{R}_0 = 2.831 H^{5/4} d^{-1/4}\sqrt{\cot(\beta)}$, $p_0 = a\sin(\theta)y - (x_0 - x_1)\cos(\theta)$, $x_0 = d\cot(\beta)$ and $a = \sqrt{1 + H/d}$.

Here, $\mathcal{R}(y)$ is the runup distribution along the local coordinate y (representing the linear coastline),

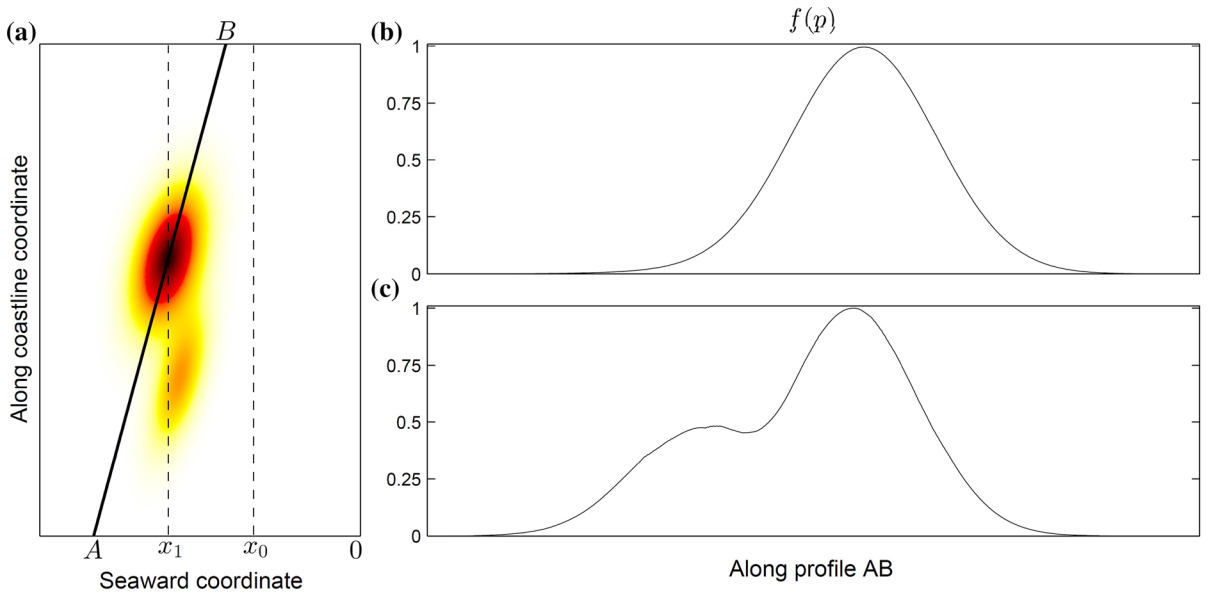

Figure 3
Construction of the analytical solution. **a** Example of an initial wave (*top view*). Idealized linear coast is at $x = 0$. **b** Decay function constructed from a cross section following the strike angle thought the maximum uplift point (RIQUELME *et al.* 2015). **c** Decay function constructed as the envelope of the whole orthogonal projection of the initial wave in a vertical plane over the coastline, with respect to the strike angle

θ is the incident tsunami angle, d the average seafloor depth, β the average beach slope angle, (x_1, 0, H) the coordinate where the maximum height of the initial wave takes place, and $f(p)$ a function in the range [0, 1] that imposes a decay along the transverse direction, allowing complexity and finiteness of the initial condition.

This modeling approach was used for the first time in RIQUELME *et al.* (2015). The authors proposed a methodology to retrieve all the parameters needed to evaluate Eq. (1) from the FFM and the bathymetry. They defined a decay function taking a cross section along the maximum uplift zone. Here, we improve upon that technique by including the whole effects of the initial condition, taking the orthogonal projection of the initial uplift, thereby respecting the directivity of the tsunami to the coast. To do this, a vertical plane is defined along the linear coast; then, at every point $\boldsymbol{v}_1$, the vertical static displacement is mapped into this plane by its orthogonal projection, that is to say,

$$\boldsymbol{v}_t = \boldsymbol{v}_0 + \langle \boldsymbol{v}_1 - \boldsymbol{v}_0, \boldsymbol{n} \rangle \boldsymbol{n},$$

where $\boldsymbol{v}_0$ and $\boldsymbol{n}$ are a given point of the plane and its normal unitary vector, respectively.

Without loss of generality, $\boldsymbol{v}_0$ can be set as $\bar{0}$. To respect the incidence of the tsunami to the coast, the normal vector is defined as $\boldsymbol{n} = (\sin\theta, -\cos\theta, 0)^t$.

Orienting with the strike angle relative to the computation domain and normalizing, we obtain the function $f(p)$ as the envelope of the resulting projection (Fig. 3).

3.3. Field Observations

In the days following the Illapel earthquake, we measured tsunami heights along the rupture region in areas directly exposed to the open ocean (following SUGAWARA *et al.* 2008). The highest pervasive marks left by vegetation razed by the tsunami, traces of erosion on the beach, and sand and boulder deposits were recorded. To estimate tsunami heights with respect to sea level, the measurements were compared to tidal variations reported by the Navy Hydrographic and Oceanographic Service (Servicio Hidrográfico y Oceanográfico de la Armada, SHOA, http://www.shoa.cl) during the earthquake. Since we used a 1 m precision barometric altimeter, calibrated at the moment of each measurement in the field, we

Table 2

Run-up measurements along the affected Chilean coast

Longitude (°)	Latitude (°)	Run-up (m)	Location name
−71.47424	−32.33457	3.07	Pichicuy
−71.535304	−32.135242	3.86	Pichidangui
−71.513554	−32.026045	4.86	Caleta Totoralillo Sur
−71.513566	−31.932249	5.47	El Quereo
−71.521082	−31.923235	5.47	Los Vilos
−71.55445	−31.638362	5.85	Huentelauquen
−71.5696	−31.51137	4.12	Puerto Manso
−71.593265	−31.422602	5.34	Puerto Oscuro
−71.643059	−31.217328	4.44	Caleta Sierra
−71.700964	−30.734914	4.55	Río Limarí (River mouth)
−71.69436	−30.54667	8.65	Caleta El Sauce (beach)
−71.6899	−30.49392	11.385	Caleta Talcacura
−71.658327	−30.305928	8.08	Punta Lengua de Vaca (beach)
−71.477583	−30.231703	3.92	Puerto Velero
−71.403223	−30.015713	5.435	Punta Panul
−71.33604	−29.953128	6.47	Coquimbo
−71.292492	−29.824801	2.01	Punta Teatinos

assigned an error of ±0.5 m for these observations (Table 2).

We observed two areas of peak tsunami heights associated with the two main rupture patches, one reaching 6 m just to the south of the epicenter and the other reaching as high as 10–11 m to the north of the epicenter (Figs. 5, 6). The maximum run-up measured was 11.4 m, located in Caleta Talcacura (−71.6899°, −30.4939°). Aránguiz *et al*. (2016) and Contreras-Lopez *et al*. (2016) have also measured the run-up along the affected coastline, finding consistent values with those obtained by our fieldwork, with peaks of 10.75 and 13.60 m, respectively.

The tsunami reached the coast no more than 5–7 min after the earthquake according to witnesses along the epicentral zone. We note that this kind of observation is biased by the duration of shaking at the observation location, which makes it somewhat subjective, but nevertheless it provides a semi-quantitative data point to judge our inversions against.

4. Tsunami Run-up Inversion

To better compare the inverted models, we generate a finite fault model based on the inversion of observed run-up data. Piatanesi *et al*. (1996) proposed a method to retrieve the FFM of the 1992 Nicaragua earthquake by inverting the run-up field observations. Here, we use this method with slight differences.

We define a discretized fault plane of 280 km along the strike and 141 km along the dip (which gives a surface $S = 39.480\text{km}^2$), with the southern-western corner located at 72.5W, 32.5S. The strike and dip are taken from the FFM solution reported by the USGS, namely 4° and 19°, respectively, with an imposed magnitude of $M_W = 8.4$. To maximize the tsunami excitation, we set the rake as 90°. The fault is segmented into $n_x = 5$ sub-faults along the strike and $n_y = 3$ sub-faults along the dip.

With a mean rigidity of $\mu = 35$ GPa, the derived average slip is $D = 2.95$ m. Notice that D is easily obtained from the relation $M_0 = \mu SD$, where M_0 is the seismic moment associated with the magnitude M_W. Therefore, allowing $(n + 1)$ possible values of slip for each cell $c_j = \frac{j}{n} N_s D$, with $j = 0, \ldots, n$ (zero slip up to all the seismic moment concentrated in one cell), this entails $\binom{n + Ns}{Ns - 1}$ different source configurations, with $N_s = n_x n_y$ the total number of cells. Notice that a fine slip step implies large values of n; thus, the number of configurations becomes untreatable. Nonetheless, we impose a maximum value of slip $D_{\max}$ in each cell, given by the Plafker rule, which states that if there are no abrupt changes in

topography along the coastline, the amplitude of maximum runup is of the order of the maximum slip on the fault and cannot be more than twice the peak slip at the source (PLAFKER 1997). We obtain the corresponding index $n_{\max} = \frac{nD_{\max}}{N_s D}$. Then, to explore all the configurations we employ an algorithm to search all the compositions of the number n with N_s parts, each part bounded by $n_{\min} = 1$ and $n_{\max}$, that is to say non-zero slip up to $D_{\max}$ (VAJNOVSZKI 2014). This reduces the computational time immensely. The number of configurations explored is

$$N_t = \sum_{k=0}^{N_f} (-1)^k \binom{Ns}{k} \binom{n_k}{N_S - 1},$$

where $N_f = \frac{n - N_S n_{\min}}{\Delta N}$, $n_k = n - (n_{\min} - 1)N_S - k\Delta N - 1$ and $\Delta N = n_{\max} - n_{\min} - 1$.

Here, a total of 459,177,855 possible cases were reduced to 2,538,294. This ensures that the average slip over the fault plane is D.

The numerical Greens functions $G_{ij}(t)$ are calculated with NEOWAVE. They correspond to the tsunami time series of the jth sub-fault at the coastal point i. They are computed in 6 h (and, as discussed above, can be pre-computed). This is enough time to include the possible effects of edge waves. Therefore, the slip distribution that we will obtain from the run-up inversion will include these effects.

We use $N = 17$ run-up measurements R_i to perform the inversion, which are compared with the peak nearshore tsunami amplitude (PNTA), for a given amplification factor a:

$$PNTA_i = a \max_{t \in [0, T_f]} \left\{ \sum_{j=1}^{N_s} c_j G_{ij}(t) \right\},$$

where T_f is the total time of the tsunami simulation and c_j the amount of slip in the jth sub-fault. The amplification factor a was varied from 2.5 to 4.0 with an incremental step of 0.05. The optimal configuration is searched numerically by minimizing the residual sum of squares:

$$Q = \sqrt{\frac{1}{N} \sum_{i=1}^{N} (R_i - PTNA_i)^2}.$$

The minimum value of Q, (namely $Q_{\min}$,) defines the final source configuration, which is shown in Fig. 4.

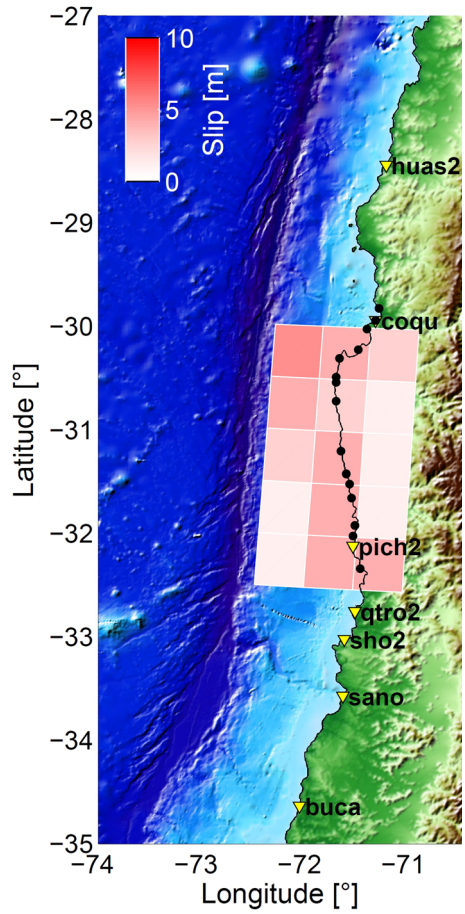

Figure 4
Slip distribution obtained from an inversion of run-up field observations (Table 2)

5. Results

We have tested three FFMs inverted with different data types (two contributed solutions, plus our own inversion of tsunami field observations). To compare them, for each model we compute the RMS between the field measurements and both the numerical run-up and the analytical solution:

$$\mathrm{RMS} = \sqrt{\frac{1}{N} \sum_{i=1}^{N} (Obs_i - \mathrm{Model}_i)^2}.$$

The USGS Finite Fault Model does not match the observed run-up along the northern portion of the coast (Fig. 5). Nevertheless, the agreement between

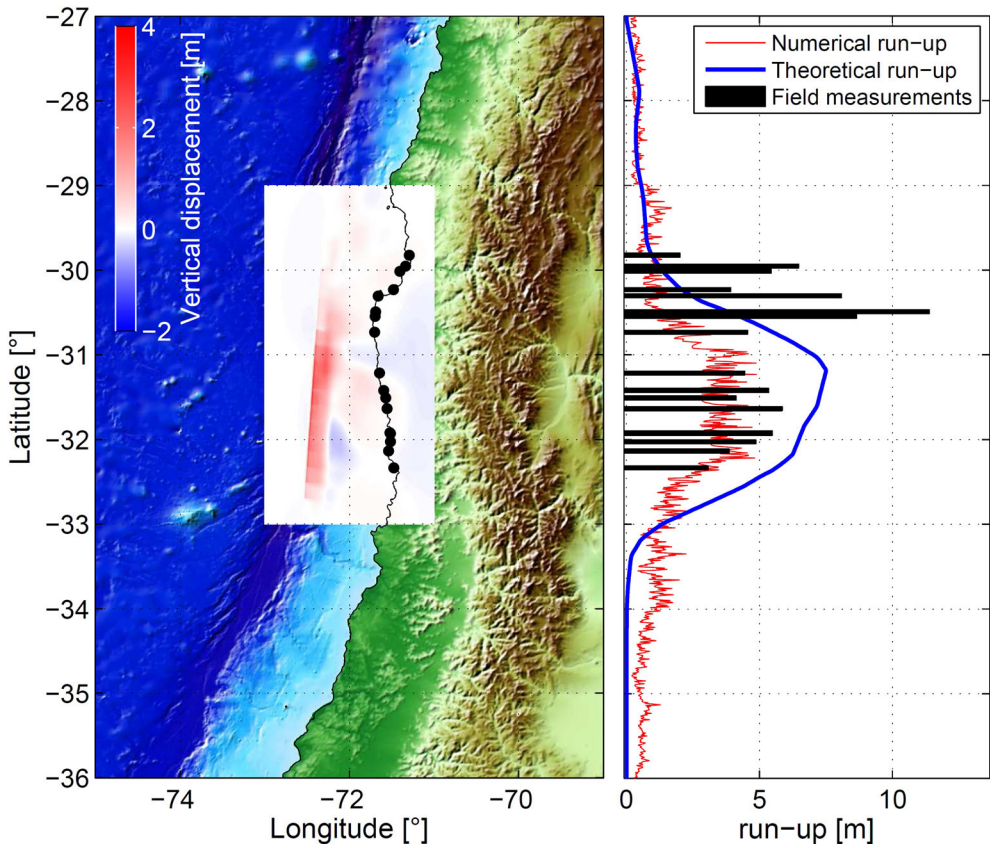

Figure 5
Comparisons of tsunami modeling approaches with field observations, using the USGS FFM. **a** Vertical static co-seismic displacement used as the initial condition for tsunami modeling. **b** Modeled run-up distribution from the two different approaches studied, numerical and analytical, compared to field measurements

the numerical and analytical solutions is remarkable (analytical solution RMS = 3.43; numerical solution RMS = 3.88). This also reflects how accurate the analytical approach is when the source shows complexity (variable slip), and when such complexity is incorporated in the solution. In this case, both the analytical and numerical solution match with Plafker's rule. However, significant slip in this model is extended southward at the trench, which does not match the run-up observations, leading us to believe that this extension may be an artifact of the source inversion.

The model of Melgar *et al*. (2016) has an RMS of 2.11 with the numerical solution and RMS = 2.62 in the analytical case. This model presents an important RMS reduction in both approaches, in agreement with the observation that incorporating multiple types of data can lead to an improved FFM and consequently a better tsunami initial condition (Fig. 6). We also note that Melgar *et al*. (2016) used refined, three-dimensional source geometry for their model, in comparison to the planar solutions employed for both the USGS model and our own run-up inversion. Such a change has also been shown to result in an improved FFM and in turn an improved tsunami model (e.g., Moreno *et al*. 2009; Hayes *et al*. 2013; Hayes et al. 2014).

In the case of the run-up inversion, the optimal source was found at $Q_{\min} = 1.58$. The Piatanesi *et al*. (1996) method works well for moderate-sized tsunamigenic earthquakes; however, there are problems when using a finer model resolution, because the solutions space becomes too big. The RMS from the numerical approach is 4.04, while the analytical case

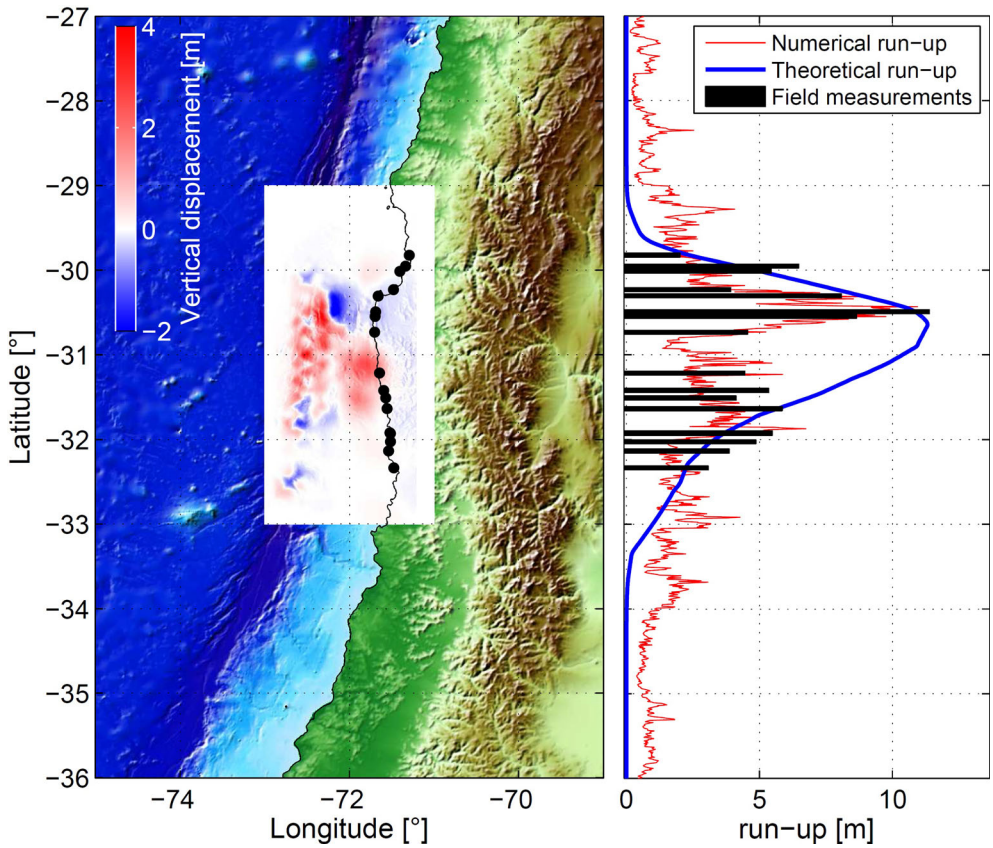

Figure 6
Comparison of tsunami modeling approaches with field observations, using the MELGAR *et al*. FFM. **a** Vertical static co-seismic displacement used as the initial condition for tsunami modeling. **b** Modeled run-up distribution from the two different approaches studied, numerical and analytical, compared to field measurements

produces an RMS of 2.74. As the Plafker rule states, one should expect maximum slip (5.4 m) to be in the order of the maximum run-up (11.4 m). Although the method provides a source that represents the mean shape of the run-up distribution, it fails to capture the finer details because of lack of resolution (Fig. 7). Due to the large size of the sub-faults used (56 km along strike and 47 km along dip), the slip distribution appears smoother than the others inversions used in this work.

The optimal amplification factor obtained using the run-up inversion method is $a = 3.90$, which is higher than the one obtained in the Nicaraguan study $a = 3.45$ (PIATANESI *et al*. 1996). This increase in amplification factor is interpreted as the Illapel tsunami impact zone being prone to having higher wave excitation.

It is also remarkable that this simple method confirms a well-known fact that uniform slip models are not suitable for modeling near-field tsunamis. Evaluating this special case (that is to say, testing the source configuration that has the same value of slip $c_j = D$ in all the sub-faults) gives a $Q_{\min} = 2.58$. However, if we use the optimal heterogeneous slip distribution, we obtain $Q_{\min} = 1.58$; a reduction of almost 40 %.

6. Discussion and Conclusions

An improvement of the analytical method discussed in RIQUELME *et al*. (2015) is presented here to accurately estimate the run-up as soon as we have an FFM. Our adapted approach takes the whole

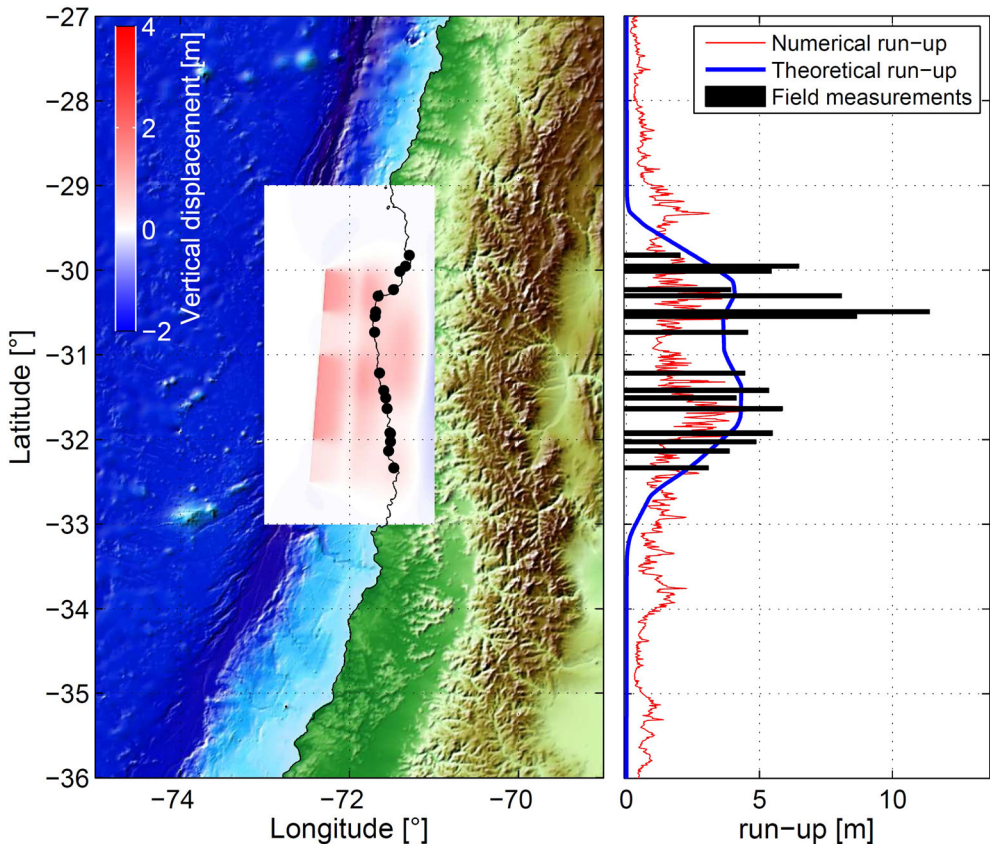

Figure 7
Comparison of tsunami modeling approaches with the field observations, using the run-up inversion FFM. **a** Vertical static co-seismic displacement used as the initial condition for tsunami modeling. **b** Modeled run-up distribution from the two different approaches studied, numerical and analytical, compared to field measurements

orthogonal projection of the tsunami initial condition, respecting the directivity to the coast, and allows us to accurately evaluate the analytical formula, capturing effects from the initial wave that were neglected in the previous study.

Run-up observations, their inversion, contributed and validated finite fault models, and the comparison of this information to observations from the Beck *et al.* (1998) study indicate that the 2015 Illapel earthquake is unlikely to be a repeat of the 1943 event. Thus, it is very important to identify if there is still enough energy stored along the subduction interface to generate an earthquake that could in turn produce a large tsunami. This is important not just for Chile, but should also be a subject of study for other regions with a tsunamigenic earthquake history, but where such earthquakes have not occurred in 100 years or more.

Our results also show that, even if the amplitude of the run-up is controlled dominantly by the source, the short tsunami arrival time is controlled more by the trench-to-coast distance and the down-dip limit of slip, rather than by the details of the rupture.

Both contributed FFMs show good agreement between the numerical and analytical run-up calculations. We find the most accurate match to run-up observations comes from the inversion that uses multiple types of data (tsunami gauges, InSAR, strong motion, hr-GPS), improved azimuthal coverage of data, and data with different frequency content, associated with different details of the resulting fault model. This is in agreement with the checkboard tests of Melgar *et al.* (2016) that illustrate different data sets have resolution of different parts of the fault plane; thus combining them

maximizes the resolution of slip over the whole fault surface. The USGS model produces good agreement between the analytical and numerical run-up predictions (Fig. 5). However, neither of those approaches can reproduce the observed run-up as well as the Melgar *et al*. (2016) model. This is predominantly because the teleseismic inversion from USGS is a rapid, operational solution and uses data from only one source: broadband seismometers. Thus, the inversion uses less input data (and thus lacks azimuthal coverage, near-field records, and data variability) compared to the Berkeley model. Nevertheless, given that this is an operational solution, what can be done in real time with the analytical model is remarkable. While it is possible to better constrain the teleseismic inversion (by choosing data with better signal to noise ratio, applying different filters, adjusting modeled geometry, etc.), since we are exploring a real-time approach with the analytical model, it is worthwhile showing what can be done in "simulated" near-real time. The Berkeley solution is more accurate, but is produced well behind real time, with the benefit of multiple data collection. Therefore, there is a trade-off between accuracy and speed. Our focus must therefore be to make the datasets used in the Berkeley model available as quickly and as accurately as possible, so these two approaches can be followed on comparable time scales.

Our own inversion of run-up data does not have resolution of the details of the slip distribution, because of the necessary coarseness of the model, but gives us an approximate idea of where the slip is concentrated, in agreement with both finite fault solutions. This method can be applied without records from tide gauges, DART buoys, GPS data, nor accelerometers or broadband seismometers.

Further work is needed to explore more theoretical aspects of the run-up problem. We have shown here that we can better estimate a run-up distribution after an FFM by including more complex features of the initial wave, gaining accuracy without sacrificing speed.

Acknowledgments

This work was entirely supported by the Programa de Riesgo Sísmico (PRS).

References

Aránguiz, R., González, G., González, J., Catalán, P. A., Cienfuegos, R., Yagi, Y., Okuwaki R., Urra L., Contreras K., Del Rio I., and Rojas, C., (2016). *The 16 September 2015 Chile tsunami from the post-tsunami survey and numerical modeling perspectives*. Pure and Appl. Geophys., *173*(2), 333–348, doi:10.1007/s00024-015-1225-4.

Beck, S. L., Barrientos, S., Kausel E., and Reyes M., (1998). *Source characteristics of large historic earthquakes along the Chile subduction zone*. J. S. Am. Earth Sci. *11*(2), 115–129, doi: 10.1016/S0895-9811(98)00005-4.

Calisto, I., Miller, M., and Constanzo, I. (2016). *Comparison between tsunami signals generated by different source models and the observed data of the illapel 2015 earthquake*. Pure and Appl. Geophys., *173*(4), 1051–1061, doi: 10.1007/s00024-016-1253-8.

Contreras-López, M., Winckler, P., Sepúlveda, I., Andaur-Álvarez, A., Cortés-Molina, F., Guerrero, C. J., Mizobe C.E., Igualt F., Breuer W., Beyá J.F., Vergara H., and Vergara, H. (2016). *Field survey of the 2015 Chile tsunami with emphasis on coastal wetland and conservation areas*. Pure and Appl. Geophys., *173*(2), 349–367, doi: 10.1007/s00024-015-1235-2.

Fuentes, M., Ruiz, J., and Cisternas, A., (2013). *A theoretical model of tsunami runup in Chile based on a simple bathymetry*. Geoph. J. Int., *196*(2), 986–995, doi: 10.1093/gji/ggt426.

Hayes, G. P., Bergman, E., Johnson, K. L., Benz, H. M., Brown, L., and Meltzer, A. S. (2013). *Seismotectonic framework of the 2010 February 27 M_w 8.8 Maule, Chile earthquake sequence*. Geoph. J. Int., *205*(3), doi: 10.1093/gji/ggt23.

Hayes, G. P., Herman, M. W., Barnhart, W. D., Furlong, K. P., Riquelme, S., Benz, H. M., Bergman, E., Barrientos, S., Earle, P.S., and Samsonov, S. (2014). *Continuing megathrust earthquake potential in Chile after the 2014 Iquique earthquake*. Nature, *512*(7514), 295–298, doi: 10.1038/nature13677.

Heidarzadeh, M., Murotani, S., Satake, K., Ishibe, T., and Gusman, A. R. (2015). *Source model of the 16 September 2015 Illapel, Chile M_w 8.4 earthquake based on teleseismic and tsunami data*. Geophys. Res. Lett., *43*(2), 643–650. doi:10.1002/2015GL067297.

Ji, C., Wald, D. J., and Helmberger, D. V. (2002). *Source description of the 1999 Hector Mine, California, earthquake, part I: wavelet domain inversion theory and resolution analysis*. Bull. Seism. Soc. Am., *92*(4), 1192–1207.

Lay, T., and Kanamori H., (2011). *Insights from the great 2011 Japan earthquake*. Phys. Today *64*(12), 33, doi: 10.1063/PT.3.1361.

Lay, T., Kanamori, H., Ammon, C. J., Koper, K. D., Hutko, A. R., Ye, L., Yue, H. and Rushing, T. M. (2012). *Depth-varying rupture properties of subduction zone megathrust faults*. J. Geophys. Res.: Solid Earth, *117*(B4), doi: 10.1029/2011JB009133.

Melgar D., Fan W., Riquelme S., Geng.J, Liang C., Fuentes M., Vargas G, Allen R.M, Shearer P., and Fielding E.J (2016). *Slip segmentation and slow rupture to the trench during the 2016, M_w 8.3 Illapel, Chile earthquake*. Geophys. Res. Lett, *43*(3), 961–966, doi: 10.1002/2015GL067369.

Moreno, M.S., Bolte, J., Klotz, J., and Melnick, D. (2009). *Impact of megathrust geometry on inversion of coseismic slip from geodetic data: Application to the 1960 Chile earthquake*. Geophys. Res. Lett. *36*, doi:10.1029/2009GL039276.

Okada, Y. (1985). *Surface deformation due to shear and tensile faults in a half-space*. Bull. Seism. Soc. Am., *75*(4), 1135–1154.

Omira, R., Baptista, M. A., and Lisboa, F. (2016). *Tsunami characteristics along the Peru–Chile trench: Analysis of the 2015 M_w 8.3 Illapel, the 2014 M_w 8.2 Iquique and the 2010 M_w 8.8 Maule tsunamis in the near-field*. Pure and Appl. Geophys., *173*(4), 1063–1077, doi: 10.1007/s00024-016-1277-0.

Pacheco, J. F., and Sykes, L. R. (1992). *Seismic moment catalog of large shallow earthquakes, 1900 to 1989*. Bull. Seism. Soc. Am., *82*(3), 1306–1349.

Piatanesi, A., Tinti, S., and Gavagni, I. (1996). *The slip distribution of the 1992 Nicaragua Earthquake from tsunami run-up data*. Geophys. Res. Lett., *23*(1), 37–40, doi: 10.1029/95GL03606.

Plafker G., (1997). *Catastrophic tsunami generated by submarine slides and backarc thrusting during the 1992 earthquake on eastern Flores I., Indonesia*. Geol. Soc. Am. Cordill., *29*(5), 57.

Riquelme, S., Fuentes, M., Hayes, G. P., and Campos, J. (2015). *A rapid estimation of near-field tsunami runup*. J. Geophys. Res.: Solid Earth, *120*(9), 6487–6500, doi: 10.1002/2015JB012218.

Scholz, C. H. (2002). The mechanics of earthquakes and faulting. Cambridge university press.

Sugawara, D., Minoura, K., and Imamura, F. (2008). *Tsunamis and tsunami sedimentology*. Tsunamiites-Features and Implications, 9–49.

Tang, L., Titov, V. V., Moore, C., and Wei, Y. (2016). *Real-time assessment of the 16 September 2015 Chile tsunami and implications for near-field forecast*. Pure and Appl. Geophys., *173*(2), 369–387, doi: 10.1007/s00024-015-1226-3.

Vajnovszki, V. (2014). *An efficient Gray code algorithm for generating all permutations with a given major index*. J. Discrete Algorithms, *26*, 77–88, doi: 10.1016/j.jda.2014.01.001.

Yamazaki, Y., Kowalik, Z., and Cheung, K. F. (2009). *Depth-integrated, non-hydrostatic model for wave breaking and run-up*. Int. J. Numer. Meth. Fluids, *61*(5), 473–497, doi: 10.1002/fld.1952.

Yamazaki, Y., Cheung, K. F., and Kowalik, Z. (2011). *Depth-integrated, non-hydrostatic model with grid nesting for tsunami generation, propagation, and run-up*. Int. J. Numer. Meth. Fluids, *67*(12), 2081–2107, doi: 10.1002/fld.2485.

Ye, L., Lay, T., Kanamori, H., and Koper, K., (2015). *Rapidly estimated seismic source parameters for the 16 September 2015 Illapel, Chile M_w 8.3 earthquake*. Pure and Appl. Geophys., *173*(2), 321–332, doi: 10.1007/s00024-015-1202-y.

(Received January 18, 2016, revised April 19, 2016, accepted April 21, 2016, Published online May 11, 2016)